Arbitrary spatial mode sorting in a multimode fiber

Hugo Defienne[*] and Daniele Faccio[†]

School of Physics and Astronomy, University of Glasgow, Glasgow G12 8QQ, United Kingdom

Sorting spatial optical modes is a key challenge that underpins many applications from superresolved imaging to high-dimensional quantum key distribution. However, to date, implementations of optical mode sorters only operate on specific sets of modes, such as those carrying orbital angular momentum, and therefore lack versatility with respect to operation with an arbitrary spatial basis. Here we demonstrate an arbitrary spatial mode sorter by harnessing the random mode mixing process occurring during light propagation in a multimode fiber by wave-front shaping. By measuring the transmission matrix of the fiber, we show sorting of up to 25 transverse spatial modes of the Fourier, Laguerre-Gaussian, and random basis to an arbitrary set of positions at the output. Our approach provides a spatial mode sorter that is compact, easy to fabricate, programable, and usable with any spatial basis, which is promising for quantum and classical information science.

A spatial mode sorter transforms a given spatial mode to a specific position in a transverse plane. Such a device is typically used to decompose a complex input optical signal into a specific spatial basis. One of the simplest examples is a convergent lens, which uniquely distributes the Fourier components of incoming light across different positions in the lens focal plane. In recent years, the development of mode sorting devices has attracted much attention because of the potential that transverse spatial modes (and knowledge of how these compose a given signal) hold for implementing fundamental optical tasks [1]. In classical optics, decomposing an image in the Hermite-Gaussian (HG) basis enables, for example, improvement of image spatial resolution [2,3] and the use of a Laguerre-Gaussian (LG) basis for spatial multiplexing allows an increase of the capacity of optical communication systems [4–6]. In quantum optics, transverse spatial modes are used for producing high-dimensional quantum states [7,8] that hold potential for quantum computing and simulation [9,10], communication [11,12], and fundamental studies [13].

However, while some technologies for manipulating spatial modes of light are commercially available and widely used [14], spatial mode sorting techniques are still at their early development stage. Among them, phase flattening is a well established scheme that was originally introduced to sort LG modes of different orbital angular momentum [7,15]. This approach has the advantage of being simple to implement because it only requires a spatial light modulator (SLM) and a single-mode fiber, but it also has drawbacks [16], including that it requires one to perform d-projective measurements over time (d is the number of sorted modes) and is restricted to specific families of modes. This technique was recently extended to LG modes with different radial index [17,18] and HG modes [19], but still measuring projections over time.

More recently, full-field mode sorting systems (i.e., no projective measurements) were developed for decomposing light into LG modes. Examples range from systems using fixed diffractive optical elements [20–22] to those based on multiple phase screens programed with SLMs [23–26]. Nevertheless, these systems are currently restricted to LG modes and are challenging to implement because they require light to be reflected by a large number of phase screens for efficient sorting. This number scales as $6d + 1$ in the case of sorting d modes between arbitrary spatial bases [27]. Finally, we also note that complex scattering has been exploited for mode sorting by Fickler *et al.* [28], but with impracticalities related to a time-consuming optimization-based wave-front-shaping approach [29] to manipulate light transmitted through a very lossy layer of TiO_2.

Here we implement a simple full-field mode sorting system that can operate on any basis. For this, we leverage the complex spatial mode mixing process performed by a multimode fiber (MMF) by using a transmission matrix (TM) -based wave-front-shaping technique. The optical TM was first measured by Popoff *et al.* [30] for manipulating monochromatic light through a layer of paint and was then extended to other complex systems such as MMFs [31,32] and is also applicable to various light sources including optical pulses [33,34] and photon pairs [35]. Recently, the TM was also used to design complex linear optical networks for classical [36] and quantum [37] simulations. In our work we extend the range of applications to spatial mode sorting. Using the TM of an MMF, we report experimental and simulated results of sorting up to 25 modes and analyze the performance of our approach with examples taken from the Fourier basis, the LG basis, and a random basis.

Figure 1(a) describes an experimental setup composed of an SLM that injects structured light into a MMF and a camera that measures the output speckle images in both polarizations. The TM of the MMF (T) is measured by illuminating the SLM at normal incidence with a collimated Gaussian beam (input mode $\mathbf{k}_0$) and using a copropagating reference, as

---

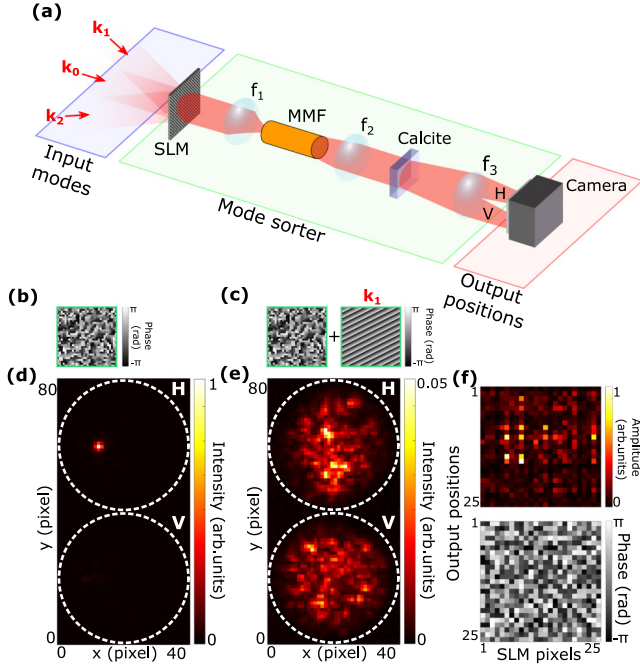[*]hugo.defienne@glasgow.ac.uk
[†]daniele.faccio@glasgow.ac.uk

FIG. 1. (a) Phase-only spatial light modulator shapes and injects monochromatic polarized light (810 nm) into a 5-cm-long 50-μm-diam-core graded-index multimode fiber using a lens $f_1 = 20$ mm. The output surface of the fiber is imaged on the camera by two lenses $f_2 = 20$ mm and $f_3 = 200$ mm. A calcite plate is used as a Wollaston prism to produce two vertical (V) and horizontal (H) polarized images next to each other. The mode sorter consists of the SLM and the MMF. Input modes are the transverse spatial modes of light illuminating the SLM and output positions are the camera pixels. (b) Phase mask programed on the SLM to focus light at normal incidence $\mathbf{k}_0$. (c) Phase ramp corresponding to an input mode $\mathbf{k}_1 \neq \mathbf{k}_0$ is superimposed onto the focusing SLM mask. Intensity images are acquired under (d) $\mathbf{k}_0$ and (e) $\mathbf{k}_1$ illuminations. (f) Amplitude and phase of a 25×25 subset of the measured transmission matrix.

detailed in [30]. The copropagating reference is a speckle pattern produced by part of the light propagating through the MMF but not modulated by the SLM. Here T is a complex matrix that links optical fields between $N = 32 \times 32$ SLM macropixels and $M = 80 \times 40$ camera pixels [Fig. 1(f)]. A Wollaston prism is positioned after the fiber to image both vertical and horizontal polarized speckle patterns on the camera and therefore double the number of spatial modes measured at the output. (See also Appendix A for more details about the TM measurement.) One of the most basic tasks that the TM can achieve is to focus light through the MMF. Using the complex conjugate operator $T^\dagger$, an SLM phase mask is calculated and programed [Fig. 1(b)] to focus scattered light at a targeted camera pixel [30], as shown in the output intensity image in Fig. 2(d). Interestingly, focusing light using the TM can be seen as a very simple one-dimensional mode sorting operation: Light from an input mode $\mathbf{k}_0$ is directed to a specific position in the camera plane. If a mode with a different wave vector $\mathbf{k}_1 \neq \mathbf{k}_0$ is inserted at the input, which is done experimentally by superimposing a phase ramp on the focusing phase mask on the SLM [Fig. 1(c)], the focusing effect at the output is lost and the mode is not sorted [Fig. 1(e)].

We build our TM-based mode sorting approach based on this method to focus light through the MMF. First, we arbitrarily choose spatial modes within a given spatial mode basis. In the example detailed in Fig. 2, we selected two modes from the Fourier basis characterized by wave vectors $\mathbf{k}_1$ and $\mathbf{k}_2$ ($\neq \mathbf{k}_0$). This basis is represented by a change-of-basis matrix P in which each column is a complex vector listing all components of the corresponding mode written in the SLM plane position basis (see Appendix B). Second, we select two positions $\mathbf{r}_1$ and $\mathbf{r}_2$ within the illuminated area on the camera and define a target mode sorting operator M. Here M is a real matrix linking input modes (column) to output positions (rows). In order to implement the sorting operation $\mathbf{k}_1 \to \mathbf{r}_1$ and $\mathbf{k}_2 \to \mathbf{r}_2$, M is written as a matrix composed of 0's with only two 1's located at the crossing between the column associated with $\mathbf{k}_1$ and the line associated with $\mathbf{r}_1$, and the column $\mathbf{k}_2$ and line $\mathbf{r}_2$. Finally, the phase mask that
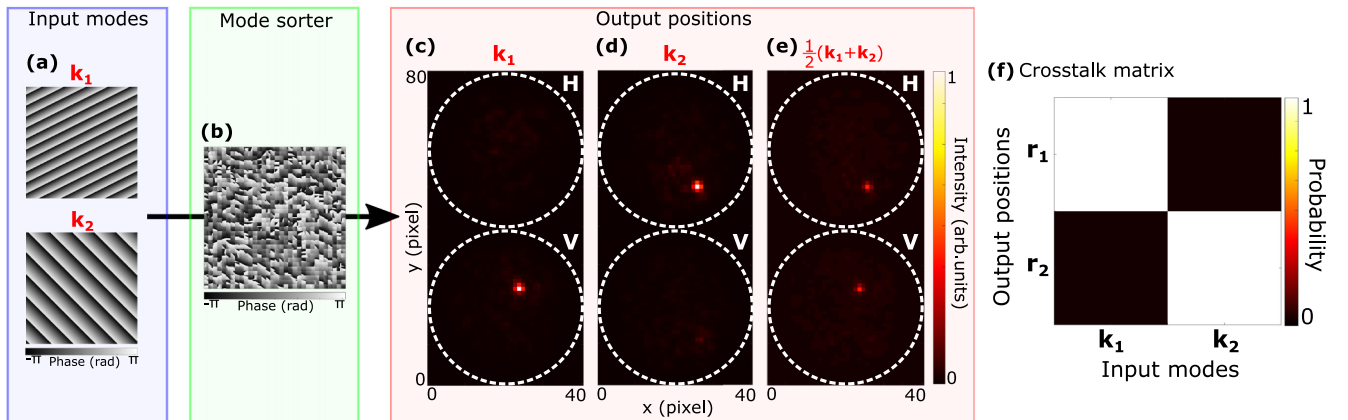

FIG. 2. (a) Spatial phase components of two input modes $\mathbf{k}_1$ and $\mathbf{k}_2$ of the Fourier basis. (b) Phase mask programed on the SLM to implement a two-dimensional mode sorter $\mathbf{k}_1 \to \mathbf{r}_1$ and $\mathbf{k}_2 \to \mathbf{r}_2$ in the MMF. Also shown are intensity images measured for (c) input mode $\mathbf{k}_1$, (d) input mode $\mathbf{k}_2$, and (e) a linear combination of them $1/2(\mathbf{k}_1 + \mathbf{k}_2)$. Light is focused in two different camera positions denoted by $\mathbf{r}_1$ and $\mathbf{r}_2$. (f) Crosstalk matrix of the programed mode sorter showing a sorting ability of 97.5(1)%.

we program on the SLM for implementing the mode sorting operation [Fig. 2(b)] is calculated using the formula [36]

$$\mathbf{\Phi} = \arg[\mathrm{diag}(T^\dagger M P^\dagger)], \tag{1}$$

where $\mathbf{\Phi}$ is a vector associated with the phase mask, diag refers to the diagonal of the matrix, and arg is the complex argument.

The physics underlying Eq. (1) can be understood when considering the propagation of the input field through the MMF. Let us first consider an ideal situation in which the SLM is replaced by an optical system that can perform the linear operation $T^\dagger M P^\dagger$, where M and P represent arbitrary target and change-of-basis matrices, respectively. The output field E^{out} obtained after propagation of an incoming field E^{in} through the MMF is then written

$$E^{\mathrm{out}} = T[T^\dagger M P^\dagger]E^{\mathrm{in}} \approx M P^\dagger E^{\mathrm{in}}. \tag{2}$$

For mode sorting, M can be written as an identity matrix and Eq. (2) then describes a change-of-basis operation between an arbitrary spatial basis and output spatial positions, namely, an arbitrary mode sorting process. Note that the approximation used in Eq. (2) directly relies on the complex spatial mode mixing process performed by the MMF. Indeed, as shown experimentally in Fig. 1(f), a subset of the TM measured in the SLM and camera pixel basis can be approximated by a random complex matrix [30,32]. In this case, one may write $TT^\dagger = \mathbb{1} + H/\sqrt{N}$, where N is the number of columns of T and H is a random matrix of complex coefficients with unity variance (see Appendix A). Equation (2) is then only valid for $N \gg 1$, which is the case in our experiment ($N = 1024$). However, in a realistic situation, an SLM can only shape the phase of the field in a specific optical plane, which means that it only controls the phase components of the diagonal coefficients of $T^\dagger M P^\dagger$. Such practical limitations effectively reduce the number of degrees of control from $2N^2$ (phase and amplitude $N \times N$ matrix coefficients) to N (phase components of an optical plane), which has the consequence of decreasing the overall efficiency of the mode sorter compared to the ideal case.

To test our mode sorter, we measured intensities at the output for input modes $\mathbf{k}_1$ and $\mathbf{k}_2$. In the experiment, input modes are generated by superimposing their corresponding phase masks on top of the mode sorting phase mask on the SLM. This approach is perfect for using a second SLM positioned in a conjugated plane ahead of the system, but only limits the sorting tests to input modes that can be produced by phase-only modulation. Figures 2(c) and 2(d) show that light focuses at the two targeted positions $\mathbf{r}_1$ and $\mathbf{r}_2$ when either of the modes $\mathbf{k}_1$ and $\mathbf{k}_2$ is inserted at the input, respectively. Moreover, Fig. 2(e) shows that light focuses on both positions simultaneously when a linear combination of modes $1/2(\mathbf{k}_1 + \mathbf{k}_2)$ is programed at the input. The mode sorting operation is characterized by a crosstalk matrix, shown in Fig. 2(f). An average sorting ability $\bar{p}$ of 97.5(1)% is calculated from the crosstalk matrix coefficients I_{nk} (nth line and kth column) using the formula $\bar{p} = \sum_{n=1}^{d} \frac{I_{nn}}{\sum_{k=1}^{d} I_{kn}}$ [28] (see Appendix C).

Figure 3 shows the results of spatial mode sorting involving up to 25 modes from different spatial basis sets. Using the same TM from the previous experiment, we calculated new
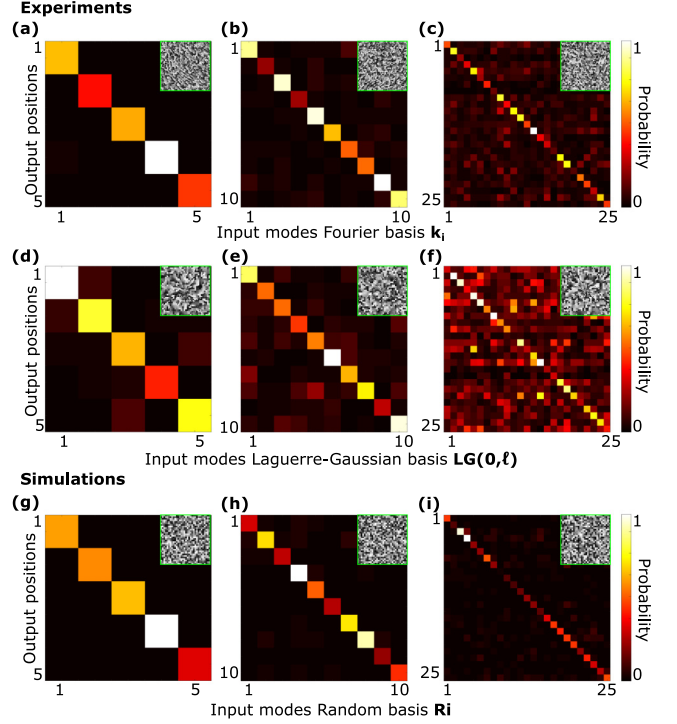

FIG. 3. Experimental results of mode sorting in the Fourier basis $\mathbf{k}_i$ ($i \in [\![1; 25]\!]$) with (a) $d = 5$, (b) $d = 10$, and (c) $d = 25$ modes. The average sorting abilities are 93(3)%, 70(9)%, and 25(10)%, respectively. Inset images show the corresponding phase masks programed on the SLM. Also shown are the experimental results of sorting Laguerre-Gaussian modes with radial number $p = 0$ and azimuthal number $\ell \in [\![-12; 12]\!]$ using (d) $d = 5$, (e) $d = 10$, and (f) $d = 25$ modes. The average sorting abilities are 82(3)%, 56(7)%, and 15(6)%, respectively. Insets show the SLM phase masks programed in each case. The results of mode sorting in a random basis $\mathbf{R}_i$ ($i \in [\![1; 25]\!]$) obtained by simulating light propagating through the MMF with an experimentally measured TM are shown for (g) $d = 5$, (h) $d = 10$, and (i) $d = 25$ modes. The average sorting abilities are 97(3)%, 83(6)%, and 45(17)%, respectively.

phase masks with Eq. (1) for three cases of sorting of $d = 5$, 10, and 25 spatial modes from the Fourier basis. Experimentally measured crosstalk matrices are shown in Figs. 3(a) and 3(b) and return values of average sorting ability ranging from 93(3)% ($d = 5$) to 25(10)% ($d = 25$). Moreover, it is essential to note that our approach can be used with any spatial mode basis. Figures 3(d)–3(f) show the results of similar mode sorting experiments performed with modes randomly chosen within a set of LG modes of radial number $p = 0$ and azimuthal number $\ell \in [\![-12; 12]\!]$. Here we recalculated the matrix P associated with the LG mode basis and the mode sorting phase masks using Eq. (1) while using the same unmodified TM. Figures 3(d)–3(f) show the measured crosstalk matrices and calculated phase masks (insets) used for sorting $d = 5$, 10, and 15 modes, with sorting ability values between 82(3)% and 15(6)%.

Using the setup shown in Fig. 1(a), the experimental tests performed to characterize a given mode sorter are limited to sets of input modes that can be created by phase-only
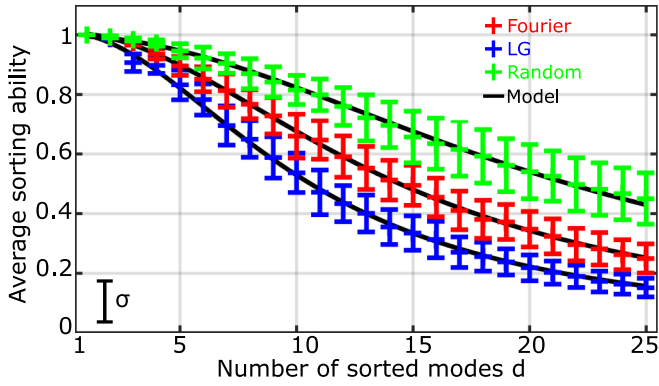
FIG. 4. Average sorting ability values for the Fourier (red middle line), LG (blue lower line), and random (green upper line) bases as a function of the number of modes d. Each value is measured by averaging over ten experiments performed with randomly chosen input modes and output positions. The results in the case of the random basis are obtained by simulating light propagation using an experimentally measured TM. The error bars represent the variations of the sorting ability values within the corresponding crosstalk matrices. Fitting models of the form $1/(1 + Ad^2) + B$ are represented by solid black lines. Fitting processes return the parameters $A = 0.005$ and $B = 0.008$ (Fourier), $A = 0.009$ and $B = 0.008$ (LG), and $A = 0.002$ and $B = -0.004$ (random), with coefficients of determination $r^2 > 0.997$.

modulation. To illustrate the versatility of our approach, we therefore simulated the results of mode sorting using a random basis in both amplitude and phase. A set of modes $\mathbf{R}_i$ with $i \in [\![1; 25]\!]$ was selected from a numerically generated random complex Hermitian unitary 1024×1024 matrix (see Appendix B). This matrix was used as P in Eq. (1) together with an experimentally measured TM T to calculate the mode sorting phase masks. Propagation through the MMF was then numerically simulated by multiplying the phase-shaped input fields by the experimentally measured TM. The results of crosstalk matrices and phase masks are shown in Figs. 3(g), 3(h), and 3(i) for $d = 5$, 10, and 25 random modes, respectively, with average sorting ability values ranging from 97(2)% to 45(17)%. These results confirm that our approach can be used to sort spatial modes from any arbitrary basis, independently of their complexity.

Finally, a quantitative analysis of mode sorting performance is provided in Fig. 4. Values of average sorting ability are represented as a function of the numbers of sorted modes d for the Fourier (red), LG (blue), and random (green) bases. Experimental and simulated values are in very good agreement with a model of the form $1/(1 + Ad^2) + B$, where A and B are two fitting parameters (see Appendix C). These results show that the average sorting ability decreases with the increase of the number of sorted modes. We also observe that the variations of sorting abilities (error bars in Fig. 4) become larger for high-d values. However, it is important to note that the average focusing enhancement in our experiment is only 89, a value that can be improved by using an MMF supporting more modes (i.e., with a larger core diameter) and controlling more SLM macropixels. Improving the ability to focus light will decrease the value of the slope parameter A and would

enable one to sort a larger number of modes with better sorting ability (see Appendix C).

In conclusion, we implemented an arbitrary spatial mode sorter in a multimode fiber using a TM-based wave-front-shaping technique. Once the TM of the MMF has been experimentally measured, it is used for sorting up to 25 modes from a Fourier, LG, or random basis. The sorting ability scales as $1/d^2$ with the number of sorted modes d. While an arbitrary mode sorting system would require $6d + 1$ programable phase screens to sort d modes [27], our approach bypasses this constraint by harnessing the complex mixing process of an MMF using wave-front shaping, at the cost of a loss in overall efficiency. Indeed, only up to 20% of the input intensity is sorted into the desired output positions (see Appendix A). This loss of efficiency results from the compromise made to be able to sort spatial modes from an arbitrary basis. Even if this value seems quite low, it is still 100 times larger than the overall efficiency obtained by Fickler *et al.* [28] using a similar approach, due to our choice of using an MMF as the complex medium rather than a lossy layer of TiO_2. Of course, if a mode sorting device only aims to operate on one specific type of mode (e.g., LG modes), it is more efficient to use the other implementations already reported in the literature [20–26].

In essence, we showed that random mixing of light, usually considered as a drawback for imaging and communication, can be turned into an advantage for spatial mode sorting applications. In this respect, the TM approach is a perfectly adapted tool because it enables one to implement any arbitrary mode sorting operations after a single measurement of the TM and until the MMF decorrelates, which typically happens after a few days due to mechanical vibrations and temperature variations (see Appendix D). On the contrary, optimization-based approaches [26,28] require a complete optimization process to be run each single time a mode sorting task is implemented, which is very time consuming. For example, Fickler *et al.* [28] need at least 20 min for implementing a $d = 2$ mode sorter using a 50-Hz SLM and up to 4 h for $d = 7$, while it would take only 80 s for a single TM measurement, making our method more practical. Beyond mode sorting, our approach is also promising in communication schemes in which it is required to not only transport spatially multiplexed information but also to sort the information at the output, as in, for example, high-dimensional quantum communication schemes [38–40]. In particular, the ability of our system to operate on any arbitrary set of modes is relevant for sorting complex superpositions, such as mutually unbiased bases, that play a major role in quantum key distribution and entanglement certification protocols [41,42].

APPENDIX A: DETAILS OF THE TM MEASUREMENTS AND FOCUSING PROCESS

1. TM measurement

The TM of the MMF is measured using the technique detailed in Ref. [30]. At the input, the SLM is divided into $32 \times 32 = 1024$ macropixels composed of 16 pixels, each of size 8 μm. At the output, optical field values are measured on $80 \times 40 = 3200$ camera pixels by phase-stepping holography using a nonmodulated speckle as a reference. The SLM is a Holoeye Pluto NIR-II and the MMF is a 5-cm-long 50-μm-diam-core graded-index MMF from Thorlabs (model No. GIF50C).

2. Enhancement ratio

The enhancement ratio is defined as the ratio between the intensity at a target position on which light is focused and the average intensity before focusing [29]. This ratio characterizes the ability of our system to focus light through the MMF using the TM. In our experiment, we measure an average focusing enhancement value of 89 (average value taken over 25 focusing targets).

3. Overall efficiency

The overall efficiency of the mode sorter is defined as the fraction of the input intensity sorted into the desired output positions. This value is estimated by dividing the enhancement ratio of the focusing process by the total number of modes supported by the MMF. As detailed in the preceding section, the enhancement ratio is 89 and the number of modes supported by a 50-μm-diam-core graded-index MMF (Thorlabs, model No. GIF50C) is approximately 380 at 810 nm [43]. These numbers lead to a maximum overall efficiency of approximately $89/380 \sim 20\%$.

4. Approximation in Eq. (2)

We consider T as an $M \times N$ matrix composed of randomly distributed complex independent coefficients, with variance σ_T^2. The elements of $TT^\dagger$ can be written as follows.

(i) Any off-diagonal element $[TT^\dagger]_{kl}$ ($k \neq l$) results from the complex sum of N random phasors

$$[TT^\dagger]_{kl} = \sum_{n=1}^{N} t_{ln} t_{kn}^*. \tag{A1}$$

Therefore, $[TT^\dagger]_{kl}$ is also a random phasor with amplitude $|[TT^\dagger]_{kl}| = \sqrt{N}\sigma_T^2$ (i.e., random walk in the complex plane).

(ii) Any diagonal element $[TT^\dagger]_{kk}$ results from the complex sum of N real elements:

$$[TT^\dagger]_{kk} = \sum_{n=1}^{N} |t_{kn}|^2. \tag{A2}$$

Therefore, $[TT^\dagger]_{kk} = N\sigma_T^2$.

In conclusion, $TT^\dagger$ can be written as

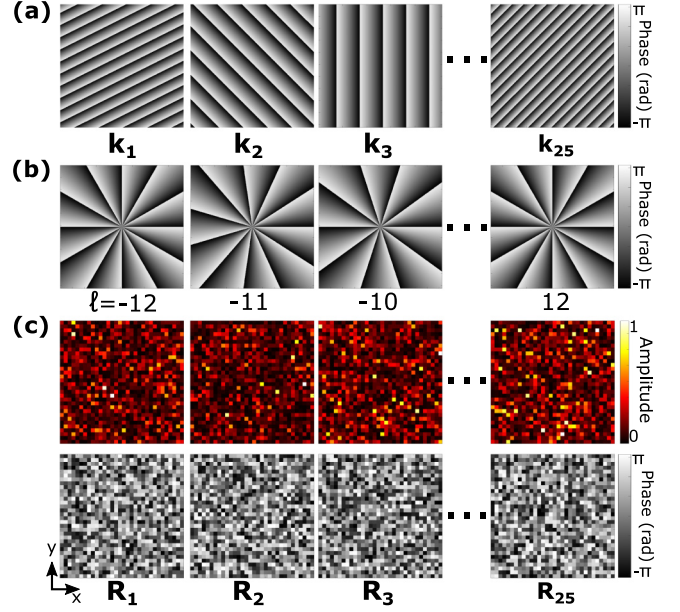$$TT^\dagger = \sigma_T^2 \left[\mathbb{1} + \frac{H}{\sqrt{N}} \right], \tag{A3}$$

FIG. 5. (a) Spatial phase component of 25 input modes selected $\mathbf{k}_i$ within the Fourier basis. (b) Spatial phase component of 25 input modes with azimuthal number $\ell_j \in [\![-12; 12]\!]$ selected in the LG basis. (c) Spatial amplitude and phase components of 25 input modes $\mathbf{R}_i$ selected in the random basis.

where H is a random matrix of complex coefficients with unity variance. Equation (2) is then only valid for $N \gg 1$, which is the case in our experiment ($N = 1024$). Note that we can write $\sigma_T^2 = 1$ by normalizing T accordingly.

APPENDIX B: DETAILS OF THE SPATIAL INPUT MODE BASIS SETS

1. Fourier basis

After spatial discretization, an element P_{ij} of the change-of-basis matrix P associated with the Fourier basis is written

$$P_{ij} = e^{i\mathbf{k}_j \cdot \mathbf{r}_i}, \tag{B1}$$

where $\mathbf{r}_i$ is the position of the ith macropixel of the SLM and $\mathbf{k}_j$ is the wave vector associated with the jth input mode. In our experiment, we selected 25 input modes with discrete wave vectors $\mathbf{k}_j = (kx_j, ky_j)$ and with values $kx_j \in \{-2.9; -1.44; 0; 1.44; 2.9\} \times 10^4$ rad m^{-1} and $ky_j \in \{-2.9; -1.44; 0; 1.44; 2.9\} \times 10^4$. The matrix P is used in Eq. (1) to calculate the mode sorting SLM phase mask. When performing the mode sorting experiments shown in Figs. 2 and 3(a)–3(c), the phase patterns associated with the corresponding input mode are superimposed on top of the mode sorting phase mask on the SLM. These phase masks are shown in Fig. 5(a).

2. Laguerre-Gaussian basis

After spatial discretization, an element P_{ij} of the change-of-basis matrix P associated with the LG basis is written

as

$$P_{ij} = e^{-|\mathbf{r}_i|^2/\omega} e^{-i\ell_j \phi_i}, \tag{B2}$$

where $|\mathbf{r}_i|$ and ϕ_i are the cylindrical coordinates of the ith macropixel of the SLM, $\omega \approx 1.7$ mm is the waist of the collimated Gaussian beam illuminating the SLM, and ℓ_j is the azimuthal number associated with the jth input mode. In our experiment, we selected 25 inputs modes with $\ell_j \in [\![-12; 12]\!]$. The matrix P is used in Eq (1) to calculate the mode sorting SLM phase mask. When performing the mode sorting experiments shown in Figs. 3(d)–3(f), the phase patterns associated with the corresponding input modes are superimposed on top of the mode sorting phase mask on the SLM. These phase masks are represented in Fig. 5(b).

3. Random basis

The change-of-basis matrix P associated with the random basis is a random complex unitary Hermitian matrix of size 1024×1024 numerically generated by a computer. We selected 25 inputs modes of this basis denoted by $\mathbf{R}_i$ with $i \in [\![1; 25]\!]$. The corresponding submatrix is used in Eq. (1) to calculate the mode sorting SLM phase mask. Amplitudes and phases of the selected modes are shown in Fig. 5(c). As explained in the main text, the results shown in Figs. 3(g)–3(i) and 4 were obtained by numerically simulating the propagation of the random input modes using an experimentally measured TM.

APPENDIX C: FITTING MODEL OF SORTING ABILITY

1. Definition of sorting ability

The sorting ability p_n associated with the nth input mode is calculated from the coefficient of the corresponding crosstalk matrix using the formula [26,28]

$$p_n = \frac{I_{nn}}{\sum_{k=1}^{d} I_{kn}}, \tag{C1}$$

where I_{kn} is the coefficient of the crosstalk matrix linking input mode n to the output position k. The average sorting ability $\bar{p}$ is therefore calculated by averaging over all the input mode sorting ability values

$$\bar{p} = \sum_{n=1}^{d} p_n. \tag{C2}$$

The associated standard deviation σ_p is calculated using the formula

$$\sigma_p = \sqrt{\frac{\sum_{n=1}^{d} (p_n - \bar{p})^2}{d}}. \tag{C3}$$

2. Fitting model

We build the fitting model of $\bar{p}$ (Fig. 4) on theoretical results already reported in [29,30]. We analyze separately the diagonal and off-diagonal coefficients of the crosstalk matrix.

(i) The SLM phase mask calculated using the TM and programed onto the SLM to implement a d-dimensional mode sorting operation results from the superposition of d phase masks, each mask being the phase pattern used for focusing
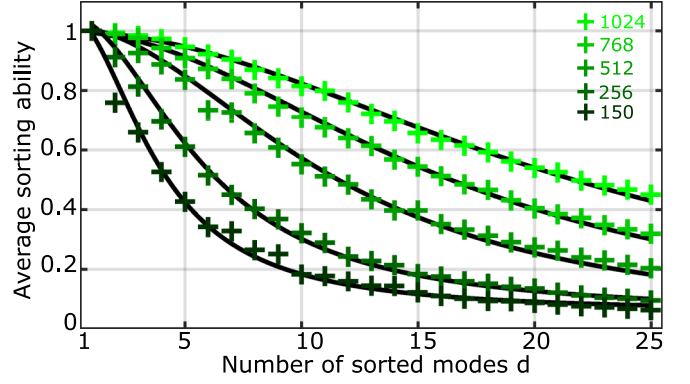

FIG. 6. Simulated average sorting ability values for random basis mode sorting are shown as a function of the number of modes d using a different number of active macropixels on the SLM. Curves, from top to bottom, are associated with $N = 1024$, which returns a coefficient of $A = 0.002$; $N = 768$, which returns a coefficient of $A = 0.004$; $N = 512$, which returns a coefficient of $A = 0.008$; $N = 256$, which returns a coefficient of $A = 0.03$; and $N = 150$, which returns a coefficient of $A = 0.06$.

light at a given position on the camera when the SLM is illuminated with a given input mode. Such a phase mask superposition is analogous to the phase mask superposition process used for focusing light through a complex system at multiple positions with an SLM illuminated by a single constant mode. In this latter case, it is demonstrated that the focusing intensity decreases as $1/d$, with d the number of target positions [29,30]. By analogy, we conclude that the diagonal coefficients of the crosstalk matrix scale as $I_{nn} \sim 1/d$.

(ii) The average intensity of the crosstalk matrix off-diagonal coefficients equals that of the grains in the output speckle pattern [29]. This average intensity value is constant. Therefore, their sum scales as d.

We therefore conclude that

$$\bar{p} = \frac{1}{d} \sum_{n=1}^{d} \left[\frac{I_{nn}}{I_{nn} + \sum_{k \neq n} I_{kn}} \right] \sim \frac{1}{1 + Ad^2}, \tag{C4}$$

where A is a coefficient that depends on the focusing efficiency of our system, which includes the number of active macropixels of the SLM. The black curves shown in Fig. 4 are obtained by fitting the experimental data with a model of the form $\frac{1}{1+Ad^2} + B$, where $\{A, B\}$ are the fitting parameters.

3. Dependence of A with the number of active macropixels on the SLM

The dependence of the parameter A with the number of active macropixels on the SLM is investigated in Fig. 6. This figure shows the results of five simulations of mode sorting in a random basis performed using different numbers of active macropixels on the SLM, ranging from 1024 to 150. We observe that the value of the coefficient A, and therefore the slope of the corresponding curve, increases when the number of active macropixels decreases. This confirms that the parameter A directly depends on our ability to refocus light through the MMF.
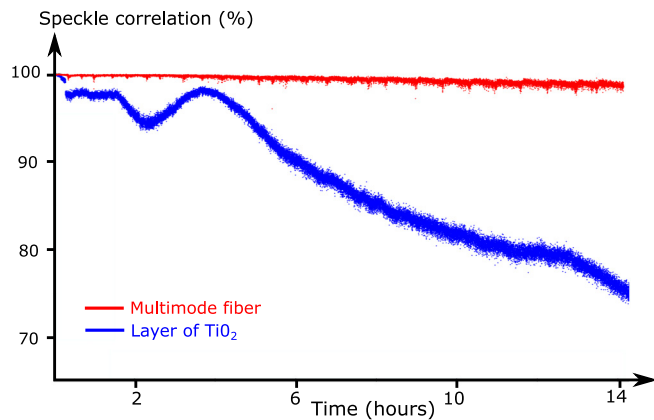
FIG. 7. Stability curves of a MMF (red) and a layer of TiO$_2$ (blue) obtained by measuring speckle correlation over time. The MMF is a 11cm-long 50 μm-diam core graded-index MMF (Thorlabs, model No. GIF50C). The layer of TiO$_2$ is a thick and dry layer of white paint positioned on a microscope slide. These stability experiments are performed by illuminating the complex system (MMF or layer of paint) with coherent light at 810 nm and measuring the speckle pattern produced at the output. Then a correlation value is calculated at time t by correlating the speckle image captured at time t with a reference speckle image taken at time $t = 0$.

APPENDIX D: STABILITY OF THE MODE SORTER

Figure 7 shows stability measurements performed using a 11-cm-long graded-index MMF (red curve) and a layer of TiO$_2$ (blue curve). These results demonstrate that the MMF is very stable (more than 97% correlation) over more than 14 h, while the layer of paint decorrelates very rapidly. Note that these two stability experiments were performed in a temperature-controlled laboratory, without putting a box around the fiber and the layer of paint. In the experimental setup described in Fig. 1, we used an MMF of the same type but twice shorter (5 cm long) and positioned inside a box, which is expected to be even more stable. Our mode sorting system is therefore stable over a characteristic time on the order of a couple of days. In practice, we were remeasuring the TM of the fiber only every two days.

APPENDIX E: DETAILS ON THE MMF AND ITS IMPACT ON THE MODE SORTING PERFORMANCE

The MMF is a 5-cm-long graded-index multimode fiber with a 50-μm-diam core from Thorlabs (model No. GIF50C). The MMF supports approximately 380 spatial modes at 810 nm. It is important to note that the number of modes supported by the fiber, which strongly influences the performance of the mode sorter, depends only on the type of fiber and its core diameter but not on its length. However, the length of the fiber still impacts the performance of the mode sorter through (a) the stability of the whole device, (b) its spectral dispersion, and (c) its overall loss.

(a) The longer the fiber, the more it is sensitive to mechanical vibrations and temperature variations. These effects can cause small modifications of the fiber structure, which will change the way light is mixed in the fiber and then its corresponding transmission matrix. If the fiber is too long, the transmission matrix will have to be regularly remeasured over time to remain valid for implementing the mode sorting. In our experiment, the MMF is a 5-cm-long fiber located inside a box and in a temperature-controlled laboratory. It is stable over a time on the order of a couple of days (see Appendix D).

(b) A different wavelength travels at a different speed through the fiber and therefore experience different mixing processes. Such a spectral dispersion effect is studied, for example, in [34] in the case of very short optical pulses propagating through MMFs. The presence of spectral dispersion reduces the ability to manipulate light propagating through the MMF by wave-front shaping and then diminishes the sorting ability and the overall efficiency of the mode sorter. In the case of (quasi)monochromatic light, the effects of spectral dispersion are only visible after propagation through very long fibers, typically of lengths on the order of kilometers.

(c) The losses in the MMF used in our experiment are around 2.3 dB/km at 810 nm. Therefore, they will have a significant impact on the overall efficiency of the mode sorter only in the case of very long fiber, e.g., kilometer-long fibers.

[1] H. Rubinsztein-Dunlop, A. Forbes, M. V. Berry, M. R. Dennis, D. L. Andrews, M. Mansuripur, C. Denz, C. Alpmann, P. Banzer, T. Bauer *et al.*, J. Opt. **19**, 013001 (2017).

[2] M. Tsang, R. Nair, and X.-M. Lu, Phys. Rev. X **6**, 031033 (2016).

[3] Y. Zhou, J. Yang, J. D. Hassett, S. M. H. Rafsanjani, M. Mirhosseini, A. N. Vamivakas, A. N. Jordan, Z. Shi, and R. W. Boyd, Optica **6**, 534 (2019).

[4] J. Wang, J.-Y. Yang, I. M. Fazal, N. Ahmed, Y. Yan, H. Huang, Y. Ren, Y. Yue, S. Dolinar, M. Tur, and A. E. Willner, Nat. Photon. **6**, 488 (2012).

[5] Y. Yan, G. Xie, M. P. J. Lavery, H. Huang, N. Ahmed, C. Bao, Y. Ren, Y. Cao, L. Li, Z. Zhao, A. F. Molisch, M. Tur, M. J. Padgett, and A. E. Willner, Nat. Commun. **5**, 4876 (2014).

[6] A. E. Willner, H. Huang, Y. Yan, Y. Ren, N. Ahmed, G. Xie, C. Bao, L. Li, Y. Cao, Z. Zhao, J. Wang, M. P. J. Lavery, M. Tur, S. Ramachandran, A. F. Molisch, N. Ashrafi, and S. Ashrafi, Adv. Opt. Photon. **7**, 66 (2015).

[7] A. Mair, A. Vaziri, G. Weihs, and A. Zeilinger, Nature (London) **412**, 313 (2001).

[8] R. Fickler, R. Lapkiewicz, W. N. Plick, M. Krenn, C. Schaeff, S. Ramelow, and A. Zeilinger, Science **338**, 640 (2012).

[9] F. Cardano, F. Massa, H. Qassim, E. Karimi, S. Slussarenko, D. Paparo, C. d. Lisio, F. Sciarrino, E. Santamato, R. W. Boyd, and L. Marrucci, Sci. Adv. **1**, e1500087 (2015).

[10] F. Brandt, M. Hiekkamäki, F. Bouchard, M. Huber, and R. Fickler, Optica **7**, 98 (2020).

[11] M. Mirhosseini, O. S. Magaña-Loaiza, M. N. O'Sullivan, B. Rodenburg, M. Malik, M. P. J. Lavery, M. J. Padgett, D. J. Gauthier, and R. W. Boyd, New J. Phys. **17**, 033033 (2015).

[12] D. Cozzolino, B. D. Lio, D. Bacco, and L. K. Oxenløwe, Adv. Quantum Technol. **2**, 1900038 (2019).

[13] M. Malik, M. Erhard, M. Huber, M. Krenn, R. Fickler, and A. Zeilinger, Nat. Photon. **10**, 248 (2016).

[14] A. Forbes, A. Dudley, and M. McLaren, Adv. Opt. Photon. **8**, 200 (2016).

[15] J. Arlt, K. Dholakia, L. Allen, and M. J. Padgett, J. Mod. Opt. **45**, 1231 (1998).

[16] H. Qassim, F. M. Miatto, J. P. Torres, M. J. Padgett, E. Karimi, and R. W. Boyd, J. Opt. Soc. Am. B **31**, A20 (2014).

[17] Y. Zhou, M. Mirhosseini, D. Fu, J. Zhao, S. M. H. Rafsanjani, A. E. Willner, and R. W. Boyd, Phys. Rev. Lett. **119**, 263602 (2017).

[18] F. Bouchard, N. H. Valencia, F. Brandt, R. Fickler, M. Huber, and M. Malik, Opt. Express. **26**, 31925 (2018).

[19] M. Hiekkamäki, S. Prabhakar, and R. Fickler, Opt. Express. **27**, 31456 (2019).

[20] J.-F. Morizur, L. Nicholls, P. Jian, S. Armstrong, N. Treps, B. Hage, M. Hsu, W. Bowen, J. Janousek, and H.-A. Bachor, J. Opt. Soc. Am. A **27**, 2524 (2010).

[21] M. P. J. Lavery, D. J. Robertson, G. C. G. Berkhout, G. D. Love, M. J. Padgett, and J. Courtial, Opt. Express **20**, 2110 (2012).

[22] G. Ruffato, M. Girardi, M. Massari, E. Mafakheri, B. Sephton, P. Capaldo, A. Forbes, and F. Romanato, Sci. Rep. **8**, 10248 (2018).

[23] G. C. G. Berkhout, M. P. J. Lavery, J. Courtial, M. W. Beijersbergen, and M. J. Padgett, Phys. Rev. Lett. **105**, 153601 (2010).

[24] M. Mirhosseini, M. Malik, Z. Shi, and R. W. Boyd, Nat. Commun. **4**, 2781 (2013).

[25] N. K. Fontaine, R. Ryf, H. Chen, D. T. Neilson, K. Kim, and J. Carpenter, Nat. Commun. **10**, 1865 (2019).

[26] R. Fickler, F. Bouchard, E. Giese, V. Grillo, G. Leuchs, and E. Karimi, J. Opt. **22**, 024001 (2020).

[27] V. J. López-Pastor, J. S. Lundeen, and F. Marquardt, arXiv:1912.04721.

[28] R. Fickler, M. Ginoya, and R. W. Boyd, Phys. Rev. B **95**, 161108(R) (2017).

[29] I. M. Vellekoop and A. P. Mosk, Opt. Lett. **32**, 2309 (2007).

[30] S. M. Popoff, G. Lerosey, R. Carminati, M. Fink, A. C. Boccara, and S. Gigan, Phys. Rev. Lett. **104**, 100601 (2010).

[31] J. Carpenter, B. J. Eggleton, and J. Schröder, Opt. Express **22**, 96 (2014).

[32] M. Plöschner, T. Tyc, and T. Čižmár, Nat. Photon. **9**, 529 (2015).

[33] M. Mounaix, D. Andreoli, H. Defienne, G. Volpe, O. Katz, S. Grésillon, and S. Gigan, Phys. Rev. Lett. **116**, 253901 (2016).

[34] M. Mounaix and J. Carpenter, Nat. Commun. **10**, 5085 (2019).

[35] H. Defienne, M. Barbieri, I. A. Walmsley, B. J. Smith, and S. Gigan, Sci. Adv. **2**, e1501054 (2016).

[36] M. W. Matthes, P. del Hougne, J. de Rosny, G. Lerosey, and S. M. Popoff, Optica **6**, 465 (2019).

[37] S. Leedumrongwatthanakun, L. Innocenti, H. Defienne, T. Juffmann, A. Ferraro, M. Paternostro, and S. Gigan, Nat. Photon. **14**, 139 (2020).

[38] N. H. Valencia, S. Goel, W. McCutcheon, H. Defienne, and M. Malik, arXiv:1910.04490.

[39] H. Cao, S.-C. Gao, C. Zhang, J. Wang, D.-Y. He, B.-H. Liu, Z.-W. Zhou, Y.-J. Chen, Z.-H. Li, S.-Y. Yu, J. Romero, Y.-F. Huang, C.-F. Li, and G.-C. Guo, Optica **7**, 232 (2020).

[40] J. Liu, I. Nape, Q. Wang, A. Vallés, J. Wang, and A. Forbes, Sci. Adv. **6**, eaay0837 (2020).

[41] D. Giovannini, J. Romero, J. Leach, A. Dudley, A. Forbes, and M. J. Padgett, Phys. Rev. Lett. **110**, 143601 (2013).

[42] J. Bavaresco, N. H. Valencia, C. Klöckl, M. Pivoluska, P. Erker, N. Friis, M. Malik, and M. Huber, Nat. Phys. **14**, 1032 (2018).

[43] B. E. A. Saleh and M. C. Teich, *Fundamentals of Photonics* (Wiley, New York, 1991).